



HAL
open science

Synthesis and Electron Accepting Properties of Two Di(benz[f]indenone)-Fused Tetraazaanthracene Isomers

Bruno Salgues, Rudraditya Sarkar, Muhammad Fajri, Yatzil Avalos-Quiroz, Anne-Doriane Manick, Michel Giorgi, Nicolas Vanthuyne, Yannick Carissan, Christine Videlot-Ackermann, Jörg Ackermann, et al.

► **To cite this version:**

Bruno Salgues, Rudraditya Sarkar, Muhammad Fajri, Yatzil Avalos-Quiroz, Anne-Doriane Manick, et al.. Synthesis and Electron Accepting Properties of Two Di(benz[f]indenone)-Fused Tetraazaanthracene Isomers. *Journal of Organic Chemistry*, 2022, 87, pp.3276 - 3285. 10.1021/acs.joc.1c02942 . hal-03594115

HAL Id: hal-03594115

<https://hal.science/hal-03594115>

Submitted on 14 Mar 2022

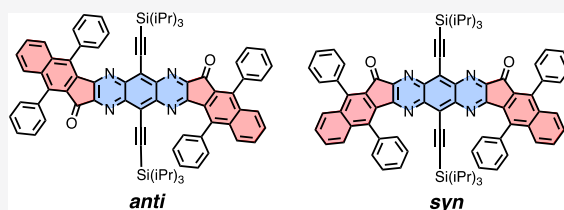
HAL is a multi-disciplinary open access archive for the deposit and dissemination of scientific research documents, whether they are published or not. The documents may come from teaching and research institutions in France or abroad, or from public or private research centers.

L'archive ouverte pluridisciplinaire **HAL**, est destinée au dépôt et à la diffusion de documents scientifiques de niveau recherche, publiés ou non, émanant des établissements d'enseignement et de recherche français ou étrangers, des laboratoires publics ou privés.

Synthesis and Electron Accepting Properties of Two Di(benz[*f*]indenone)-Fused Tetraazaanthracene Isomers

Bruno Salgues, Rudraditya Sarkar, Muhammad Luthfi Fajri, Yatzil Alejandra Avalos-Quiroz, Anne-Doriane Manick, Michel Giorgi, Nicolas Vanthuyne, Yannick Carissan, Christine Videlot-Ackermann, Jörg Ackermann, Gabriel Canard, Jean-Luc Parrain, Boris Le Guennic, Denis Jacquemin,* Muriel Amatore, Laurent Commeiras, Elena Zaborova,* and Frédéric Fages*

ABSTRACT: We designed and synthesized a novel di(benz[*f*]indenone)-fused tetraazaanthracene derivative and isolated its two isomers, **1a** and **1s**, having *anti* and *syn* configurations, respectively. Their structure and that of the condensation reaction intermediates, *anti*-**2a** and *syn*-**2s**, were fully characterized using one- and two-dimensional nuclear magnetic resonance spectroscopy and single-crystal X-ray diffraction. The optical and electronic properties of **1a** and **1s** were investigated using ultraviolet–visible absorption and fluorescence spectroscopies, cyclic voltammetry, and time-dependent density functional theory calculations. The presence of the carbonyl and ethynyltris(isopropyl)silane groups endows the di(benzindenone)-fused azaacene derivatives with a strong electron accepting character. With an electron affinity of approximately -3.7 eV, the two isomers represent attractive electron-deficient molecular systems for the generation of *n*-channel semiconducting materials. Organic field effect transistors of **1a** and **1s** showed electron transport, and organic solar cells gave a proof of concept of the potential of the two compounds as electron acceptor materials when they are paired with an electron donor polymer.



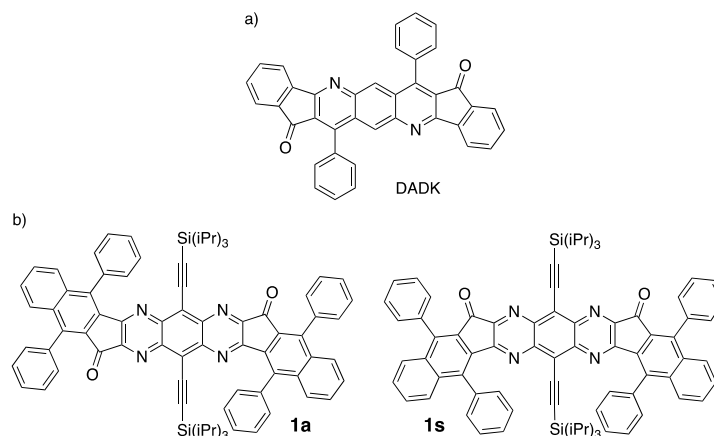
INTRODUCTION

Electron acceptor organic dyes are of great interest for applications as redox photocatalysts¹ and *n*-type organic semiconductors for the fabrication of electronic and photovoltaic devices.^{2–5} In this framework, large polycyclic N-heteroaromatics such as polyazaacenes occupy a privileged spot because of the many possibilities they offer in terms of chemical structures, functional properties, and applications, which is revealed by the considerable amount of work devoted to this broad class of compounds.^{6–8} Comparatively, bis-indenone-fused analogues have been sparsely investigated. In 2010, Jenekhe and collaborators reported what is, to the best of our knowledge, the first example of a bis-indenone-fused anthrazoline derivative, the so-called DADK (Chart 1),⁹ providing thin film materials showing significant electron mobility. Electron transport was also investigated by quantum chemical calculations.^{10,11} Compared to the bare anthrazoline core, introduction of the indenone moiety in DADK was shown to increase the electron affinity and decrease the fluorescence intensity presumably due to the intersystem crossing population of the photoexcited triplet state.⁹ Unipolar *n*-type and ambipolar organic semiconductors based on indenone-fused azaacene molecules and polymers have also been reported.^{12–14} As a further asset, indeno-fused pyrazine derivatives provided precursors of quinoidal closed-shell systems and ground-state conjugated diradicals.¹⁵ From a

more exploratory standpoint, indeno-fused acenes and azaacenes are conjugated carbonyl compounds that might be used as cathode materials in rechargeable batteries.¹⁶

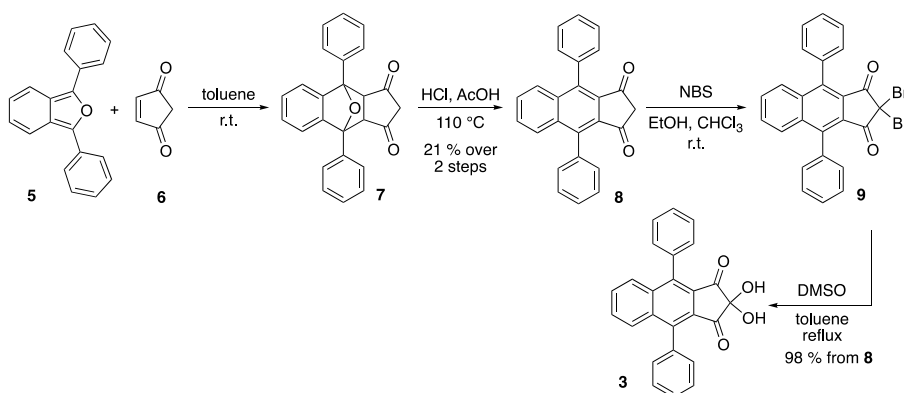
We report herein a synthesis approach toward two di(benz[*f*]indenone)-fused 1,4,5,8-tetraazaanthracene derivatives (Chart 1). The π -conjugated backbone of the two compounds consists of nine fused rings. The *meso* positions of the tetraazaanthracene core are equipped with triisopropylsilyl (TIPS)-ethynyl groups to improve the solubility in organic solvents. The two phenyl rings attached to each lateral naphthalene moieties are also expected to contribute to the enhanced solubility by limiting π -stacking interactions. Interestingly, the synthetic route described here led to the formation of the two configurational isomers, **1a** and **1s**, in which the two carbonyl functions are positioned in *anti* and *syn* relationships, respectively. We could isolate and characterize **1a** and **1s**, which allowed us to evaluate the effect of molecular symmetry on the electronic properties of those polycyclic

Chart 1. Molecular Structures of (a) Literature Compound DADK and (b) 1a and 1s Isomers Investigated in This Study

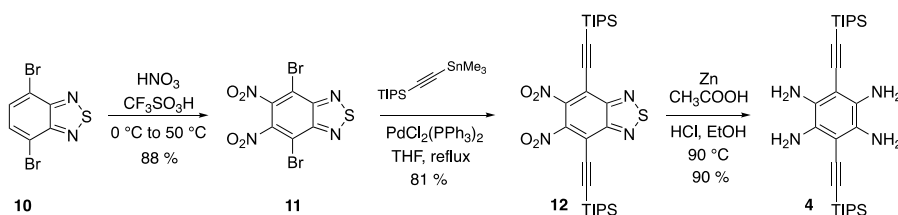


Scheme 1. Synthesis of Molecules 3 and 4

a) synthesis of 3



b) synthesis of 4



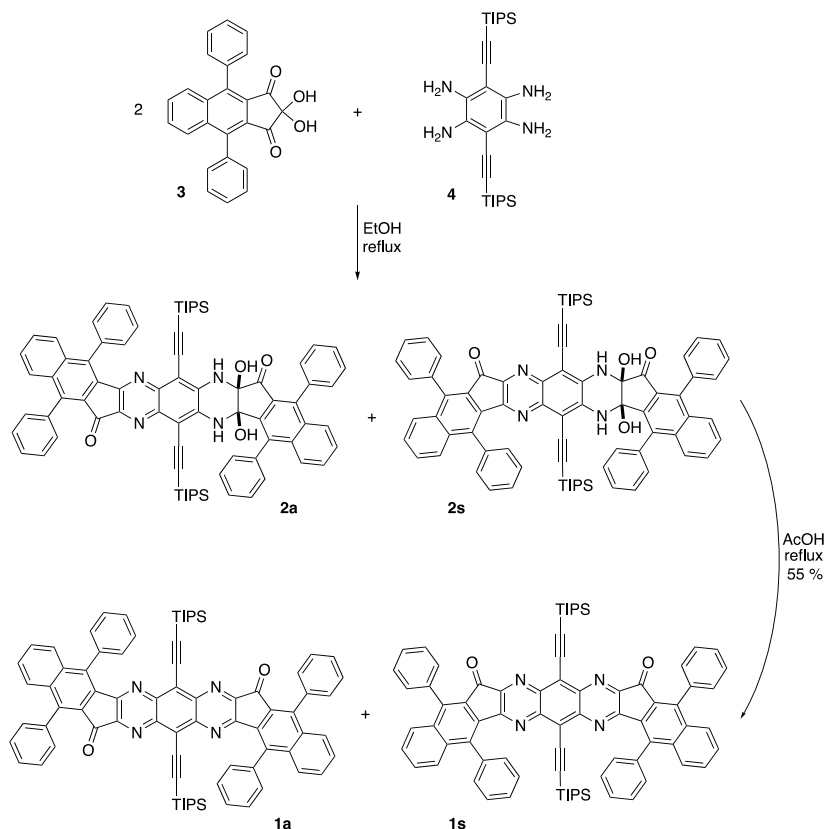
heteroaromatic compounds. Indeed, a recent study of pyrene-fused azaindene isomers showed the crucial impact of the molecular configuration on solid-state organic memory device performance.¹⁷ In the work presented here, the spectroscopic and electrochemical properties of **1a** and **1s** in solution are described. We also provide a proof of concept of the potential of **1a** and **1s** as electron acceptors in OSCs blended with an electron donor polymer. Moreover, we have isolated two bis(hemiaminal) intermediates, **2a** and **2s**, forming during the course of the condensation step involving *o*-diamine and benzo[*f*]ninhdrin precursors. The structure of **1a** and **2s** could be ascertained by one-dimensional (1D) and two-

dimensional (2D) NMR and single-crystal X-ray diffraction analysis.

RESULTS AND DISCUSSION

The construction of the di(benz[*f*]indenone)-fused tetraazaanthracene core is based on the condensation reaction between a ninhydrin derivative **3** and tetraamine **4**. The preparation of the hitherto unknown **3**, 2,2-dihydroxy-4,9-diphenyl-(1H)-benzo[*f*]inden-1,3(2H)-dione, is depicted in Scheme 1a.^{18–20} The synthesis started with dione **8**, which is already known.¹⁸ It was prepared in two steps according to the published procedure,¹⁸ namely, the Diels–Alder cycloaddition of 4-cyclopentene-1,3-dione **6** with 1,3-diphenylbenzofuran **5**

Scheme 2. Synthesis of Molecules 1a and 1s



followed by a dehydration reaction of the 1,3-diphenylbenzo-*[c]*furan-cyclopent-4-ene-1,3-dione cyclo-adduct 7 to afford **8** in 21% yield over two steps. Compound **8** gave analytical and spectral data consistent with those reported in the literature.¹⁸ Following procedures adapted from previous reports,^{19,20} dione **8** was brominated with *N*-bromosuccinimide in a 1:1 (v/v) ethanol/chloroform solvent mixture at room temperature to give **9**. This compound was found to be unstable presumably due to the sensitivity of the *gem*-dibromo function and could not be purified using standard procedures. Nevertheless, this product gave a satisfactory proton NMR spectrum (Figure S1). Therefore, it was used as obtained in the subsequent step being reacted with DMSO in refluxing toluene, which afforded ninhydrin derivative **3** (Figures S2–S5) in 98% overall yield from **8**.

The already known TIPS-ethynylated tetraamino derivative **4** was synthesized in four steps following a procedure identical to that described in the literature (Scheme 1b).^{21–24} The first step is the dinitration of 4,7-dibromo-2,1,3-benzothiadiazole **10** using nitronium trifluoromethanesulfonate as a nitrating agent (88%). The 4,7-dibromo-5,6-dinitrobenzothiadiazole **11** was then subjected to a Stille cross-coupling with 1-trimethylstannyl-2-triisopropylsilyl ethyne and bis-triphenylphosphine palladium chloride (10 mol %) in THF to give **12** in 81% yield. Compound **12** was finally reduced with zinc in ethanol in the presence of acetic acid and HCl to yield tetraamine **4** after treatment with aqueous NaHCO₃ as a base. Unstable tetraamine **4**²² was immediately condensed with hydrated triketone **3**.

The condensation reaction of **3** with **4** was performed in refluxing ethanol (Scheme 2). The use of acetic acid as a solvent was avoided to prevent the possible condensation of tetraamine **4** with acetic acid followed by the oxidative cyclization reaction, yielding an imidazole moiety as reported elsewhere.²⁵ Surprisingly, the expected 1:1 mixture of **1a** and **1s** isomers was obtained with a very low yield (5%), indicating that this reaction is not effective. Actually, the two major products (44% yield) could be isolated and were identified as a 1:1 mixture of isomers **2a** and **2s** (Scheme 2). Their asymmetrical structure features one benzoindenone fragment as expected from the condensation of **3** with one of the two *o*-diamino functions of **4**, and a bis(hemiaminal) moiety involving the second *o*-diamino group. This implies that the hemiaminal function in **2a** and **2s** could not undergo dehydration/aromatization in ethanol. No attempt was made to separate **2a** and **2s**, and spectroscopic characterizations were obtained for the mixture. In particular, the bis(hemiaminal) structure was fully confirmed using 1D and 2D NMR experiments (Figures S6–S13), high-resolution mass spectrometry (HR-MS) (Figure S14), and Fourier transform infrared spectroscopy (FT-IR) (Figure S15). The proton NMR spectrum of the mixture of **2a** and **2s** shows two sets of two sharp resonance peaks at 3.5–4.5 and 5.5–6 ppm in CD₂Cl₂. The former set could be assigned to the hydroxyl protons by D₂O exchange (Figure S7). The HMBC ¹H–¹³C NMR spectrum (Figure S12) further indicated that only the OH (NH) proton resonating at 4.25 ppm (6 ppm) long-range couples with the C=O carbon atom at 194.4 ppm, meaning

that the two isomers give rise to the same two sets of resonances. Single crystals of compound **2s** suitable for X-ray analysis could be grown by slow diffusion of pentane vapor in a dichloromethane (DCM) solution of the mixture of **2a** and **2s** (Table S1). A projection of the molecular structure is given in Figure 1. Because of the presence of the two asymmetric

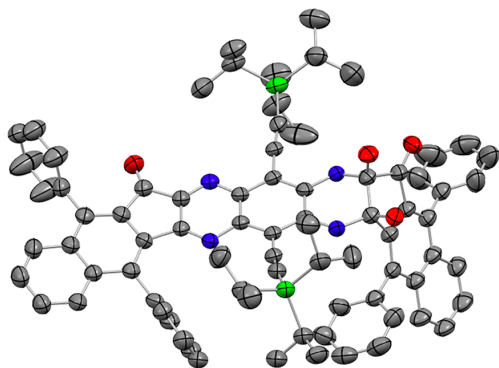


Figure 1. ORTEP view of the crystallographic structure of **2s** with 50% probability ellipsoids: red for oxygen, blue for nitrogen, and green for silicon. Hydrogen atoms have been omitted for the sake of clarity.

hemiaminal carbon atoms, **2s** exists as two enantiomers, (*R,R*) and (*S,S*), that can be found in the crystal lattice. One of the two acetylenic bonds is out of the plane of the central ring [tilt angle equal to $165.7(4)^\circ$] probably because of the pronounced steric stress induced by the two adjacent phenyl rings in the *syn* isomer. One water molecule bridges two adjacent **2s** molecules (Figure S16) through its oxygen atom to the hydrogen of the hemiaminal hydroxyl group of one molecule in the asymmetric unit and through one of its hydrogen atoms to the oxygen atom of the keto function of a symmetry-related molecule (symmetry code: $1/2 - x, 1/2 + y, 3/2 - z$). These interactions build an infinite helicoidal chain along the *b*-axis. Figure 1 shows a *cis* configuration for the junction between the five- and six-membered rings in **2s**, which is in agreement with the correlations between OH protons observed in the NOESY ^1H - ^1H NMR spectrum of the isomeric mixture in solution (Figure S13). This configuration is also well supported by DFT calculations showing that the optimized *cis* geometry of **2s** is

more stable than its *trans* counterpart by >40 kJ/mol (Figures S17 and S18).

Eventually, we found that heating the mixture of **2a** and **2s** in acetic acid as a more acidic solvent led to the mixture of **1a** and **1s** in 55% yield. While a small amount of each of the pure isomers **1a** and **1s** could be isolated via column chromatography during the initial reaction workup, quantitative separation of the larger amount of **1a** and **1s** obtained from treatment of the mixture of **2a** and **2s** required the use of preparative HPLC (Figure S19). In spite of the distinct symmetry of isomers **1a** and **1s**, their proton NMR spectra display a similar splitting pattern in the aromatic region (Figure S20) and the structure of two compounds could not be assigned straightforwardly on this basis. However, in addition to the single-crystal structure (see below), ^1H and ^{13}C NMR proved to be useful for distinguishing between the two isomers as the resonance peaks of the aliphatic TIPS atoms in *syn*-**1s** are split because of the noncentrosymmetric geometry of this isomer (Tables S2 and S3 and Figures S20 and S21). The structure of **1a** and **1s** was unambiguously confirmed through 1D and 2D NMR, HR-MS, and FT-IR (Figures S20–S37).

The ultraviolet–visible (UV–vis) absorption spectra of **1a** and **1s** recorded in DCM are displayed in Figure 2a. They show similar spectral features with an intense transition at a high energy (for **1a**, $\lambda_{\text{max}} = 394$ nm; for **1s**, $\lambda_{\text{max}} = 407$ nm) and a series of structured low-energy bands extending to the visible region. The lowest-energy transition in **1a** and **1s** appears at a similar wavelength ($\lambda_{\text{onset}} = 630$ nm), leading to an estimated optical gap value of 1.97 eV for both compounds in DCM. The molar absorption coefficient of the high-energy transition at λ_{max} is significantly larger for **1a** ($118400 \text{ M}^{-1} \text{ cm}^{-1}$) than for **1s** ($61750 \text{ M}^{-1} \text{ cm}^{-1}$). One notes, however, that the transition band in **1s** is broader and split compared to that of **1a**. The thin film UV–vis absorption spectra of **1a** and **1s** are very similar in both peaks' shape and position to their solution counterparts (Figure S38). The high-energy transition exhibits a moderate red-shift (<5 nm), while the maximum of the lowest-energy band is unchanged, giving the same 1.97 eV value for the optical gap of **1a** and **1s** in the solid state.

Both isomers were found to be weakly fluorescent in DCM with a fluorescence quantum yield of 0.03. The shape of the emission profile mirrors that of the lowest-energy transition (Figure 2b), confirming the rigidity of the di(benz[*f*]-indenone)-fused tetraazaanthracene core. This statement also

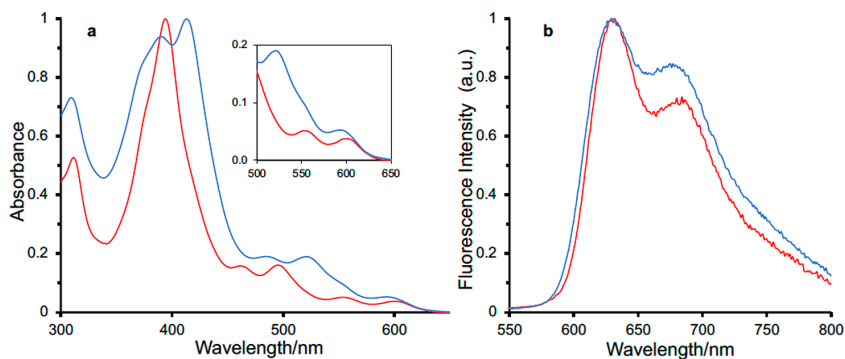


Figure 2. (a) UV–vis absorption and (b) fluorescence emission spectra of **1a** (red) and **1s** (blue) in DCM. The inset shows the lowest-energy absorption band. $\lambda_{\text{exc}} = 495$ nm for **1a** and 520 nm for **1s**. Spectral intensities are normalized to unity at the absorption or emission maximum wavelength.

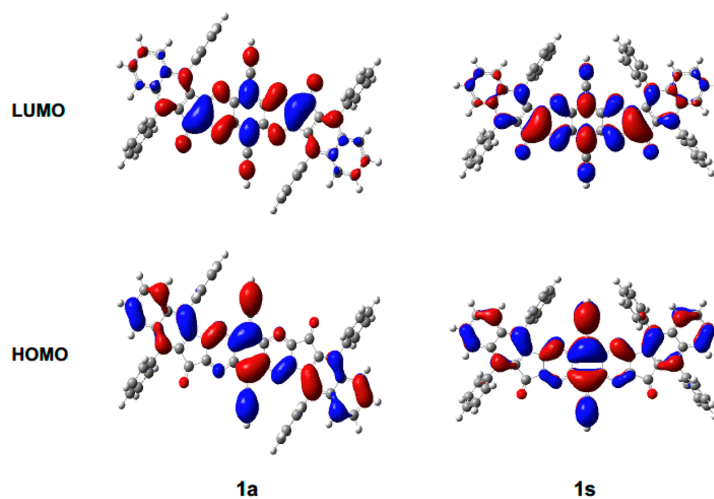


Figure 3. Shapes of frontier molecular orbitals for **1a** and **1s**. The tris(isopropyl) groups have been replaced by hydrogen atoms.

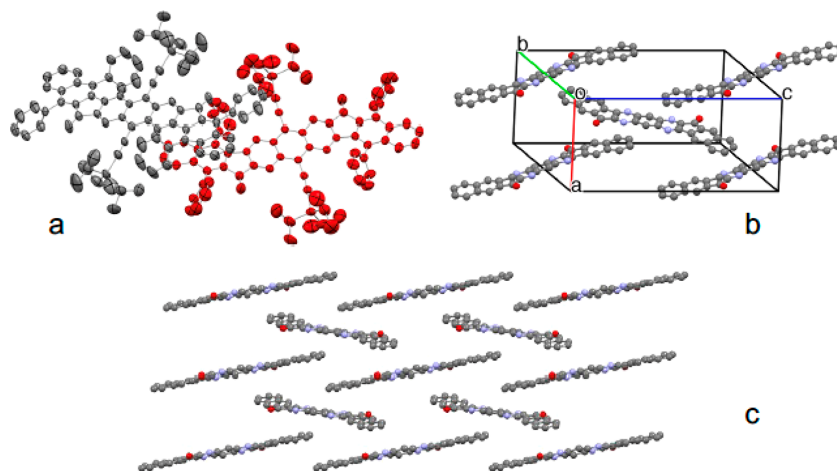


Figure 4. Single-crystal X-ray structure of **1a**. (a) ORTEP view of the two independent conformers with ellipsoids drawn at the 50% probability level. (b) View of the molecular packing of **1a** and (c) projection down the *b*-axis showing the columnar arrangement. Phenyl rings and TIPS-ethynyl substituents have been omitted in panels b and c for the sake of clarity.

agrees with the rather small Stokes shifts (for **1a**, $\Delta\nu = 780 \text{ cm}^{-1}$; for **1s**, $\Delta\nu = 990 \text{ cm}^{-1}$). The emission spectra display a vibronic structure with vibronic spacings of 1100 and 1300 cm^{-1} for **1s** and **1a**, respectively. No detectable phosphorescence emission could be recorded in frozen 2-methyl-tetrahydrofuran at liquid nitrogen temperature.

Time-dependent density functional theory (TD-DFT) calculations have been performed to gain further insights into the nature of the electronic excited states of both **1a** and **1s**. First, we note that **1a** and **1s** are found in C_i and C_2 point group, respectively. As one can see in [Tables S4 and S6](#), the lowest excited states are located at 591 and 569 nm in **1a** and **1s**, respectively, and are weakly dipole allowed. This is in line with the experimental weak absorptions at $\sim 600 \text{ nm}$ ([Figure 2](#)). These lowest-energy transitions can be attributed to a HOMO-to-LUMO excitation. The corresponding molecular orbitals are displayed in [Figure 3](#). The HOMOs are spread over the molecular backbone, including the terminal naphthalene moieties and the ethynyl bonds, whereas the LUMOs are

centered on the central tetraazaacene core and indenone units. TD-DFT calculations next indicate several relatively weakly allowed transitions in the 530 to 420 nm domain, which is also consistent with the experimental absorption. At 406 nm (**1a**) and 425 nm (**1s**), transitions with very large oscillator strengths are determined by TD-DFT, obviously corresponding to the $\sim 400 \text{ nm}$ intense peaks at [Figure 2](#). As one can see in [Tables S5 and S7](#), these transitions are highly delocalized $\pi-\pi^*$ excitations with strong overlap between the occupied and virtual orbitals. Eventually, to allow for more direct comparisons between experiment and theory, we simulated vibronic contributions for all transitions with significant oscillator strengths. The computed UV-vis spectra are shown in [Figures S39 and S40](#), and these calculations clearly indicate that the bands in the experimental spectra of [Figure 2](#) involved both several electronic states and significant vibrational coupling.

A single crystal of **1a**, grown by slow diffusion of pentane in DCM, was analyzed by single-crystal X-ray diffraction. **1a**

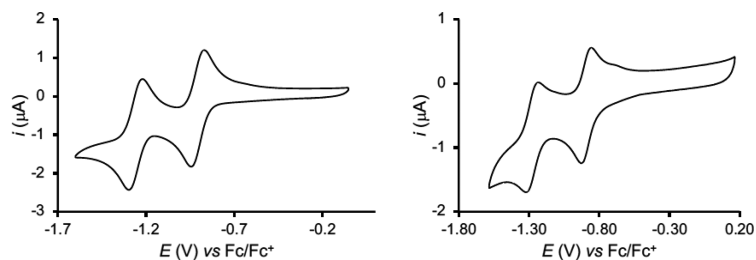


Figure 5. Cyclic voltammetry of **1a** (left) and **1s** (right) in DCM with $n\text{-Bu}_4\text{NPF}_6$ as a supporting electrolyte, a Pt working electrode, a platinum wire counter electrode, and a Ag/AgCl reference electrode. The scan rate was 100 mV s^{-1} .

crystallizes in triclinic space group $P\bar{1}$ with two independent half-molecules in the asymmetric unit (Table S1). These molecules are each located on a center of inversion and are thus centrosymmetric. They correspond to two conformers differing by the torsion angles of the peripheral phenyl rings (varying from 60° to 78°) and the amplitude of distortion from linearity observed for the TIPS segments. The crystal structure reveals that the nine fused rings form a relatively planar framework, with a largest out-of-plane distance of $<0.21\text{ \AA}$ (Figure 4a). The molecular packing diagrams in panels b and c of Figure 4 show that **1a** forms parallel interpenetrated columns along the a -axis, resulting in a kinked arrangement intermediate between herringbone and brickwall patterns. Molecules of two adjacent columns interact via their naphthalene moieties, and although the shortest intermolecular distance is typical of π -stacking ($\sim 3.2\text{ \AA}$), the molecular planes are not parallel, resulting in limited π - π overlap. This observation is consistent with the high degree of similarity between the thin film and solution UV-vis absorption spectra of both **1a** and **1s**.

The electrochemical properties of **1a** and **1s** in DCM containing 0.1 M tetrabutylammonium hexafluorophosphate ($n\text{-Bu}_4\text{NPF}_6$) were probed by cyclic voltammetry (Figure 5). The redox potential values are given versus the ferrocene/ferrocenium couple. The two compounds display two reversible one-electron reduction waves at -0.91 and -1.26 V for **1a** and -0.89 and -1.26 V for **1s**. Accordingly, the LUMO energy was calculated²⁶ and found to be close for the two isomers (**1a**, -3.70 eV ; **1s**, -3.72 eV). Because no oxidation wave could be observed under our experimental conditions, the HOMO energy was estimated from that of the LUMO level and using the optical gap value determined previously, giving -5.67 and -5.69 eV for **1a** and **1s**, respectively. At this stage, we note that the effect of the attachment of two benzoindenone units to the TIPS-ethynylated tetraazaanthracene is similar to that reported recently for an azaacenodibenzosuberone derivative.²⁷

1a and **1s** have HOMO and LUMO energies close to those of [6,6]phenyl-C61-butyric acid methyl ester (PC₆₁BM), a commonly used electron-accepting material in organic photovoltaic devices, and might therefore act as suitable acceptor materials. To ascertain this hypothesis, we built a bulk heterojunction (BHJ) OSC with an ITO/ZnO/PTB7-Th:**1a** (or **1s**)/MoO₃/Ag inverted architecture.²⁸ The active layer is a blend [50:50 (w/w)] composed of the donor polymer poly({4,8-bis[5-(2-ethylhexyl)-2-thienyl]benzo[1,2-*b*:4,5-*b'*]-dithiophene-2,6-diyl}{2-[(2-ethylhexyl)oxy]carbonyl}-3-fluorothieno[3,4-*b*]thiophenediyl)} (PTB7-Th) and **1a** or **1s** as the acceptor component. PTB7-Th was selected in this study because its HOMO (-5.24 eV) and LUMO (-3.66 eV)

levels are compatible with photoinduced charge transfer to **1a** and **1s**.²⁹ The blends were spin-coated from chlorobenzene as the solvent. The current density-voltage (J - V) characteristics are shown in Figure 6 and Figure S41, and the data listed in

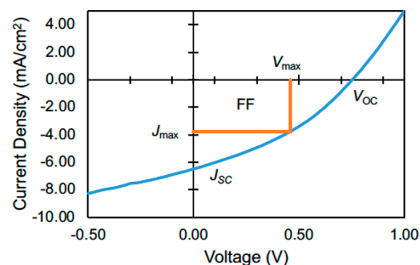


Figure 6. J - V curve under 100 mW/cm^2 illumination of a BHJ-OSC made with PTB7-Th:**1a** [50:50 (w/w)] spin-coated from chlorobenzene.

Table S8. The values of open circuit voltage V_{OC} are in the range of 0.74 – 0.78 eV , and the power conversion efficiencies (PCEs) are modest with values of $\sim 1\%$ for **1a** and $\sim 1.2\%$ for **1s**. Although the fabrication of the devices has not been optimized, the limited value of PCE reflects the relatively low value of fill factor FF and short circuit current density J_{SC} , which might stem from an insufficient electron mobility. Indeed, organic field effect transistors demonstrated unipolar n -type characteristics (Figure S42), and electron mobility values of $(2.9 \pm 1.1) \times 10^{-5}$ and $(0.84 \pm 0.11) \times 10^{-5}\text{ cm}^2\text{ V}^{-1}\text{ s}^{-1}$ for **1a** and **1s**, respectively, were extracted from the saturation regime of the transfer characteristics (Figure S43 and Table S9). Among the BHJ-SC devices prepared in this study, the best performance was obtained for **1a** with a J_{SC} of 6.49 mA/cm^2 , a V_{OC} of 0.76 V , and an FF of 0.35 , giving a PCE of 1.73% . These preliminary experiments clearly show that compounds **1a** and **1s** serve as acceptor materials when paired with PTB7-Th as a donor in a BHJ-SC.

In summary, the two isomers **1a** and **1s** of a TIPS-ethynylated di(benz[*f*]indenone)-fused tetraazaanthracene derivative have been synthesized and characterized, which involved the preparation of a new ninhydrin derivative **3**. They display similar spectral and electrochemical properties, leading to similar values of HOMO/LUMO energy levels. A theoretical investigation confirmed the trend observed in the experimental UV-vis absorption spectra showing that the effect of molecular symmetry on optical properties in solution is finally rather moderate. The electrochemically measured LUMO energies confirm the marked electron accepting character of the TIPS-ethynylated di(benzoindenone)-fused

tetraazaanthracene core in both isomers **1a** and **1s**. With a conjugated backbone composed of nine fused rings, these compounds display a reasonable solubility in organic solvents allowing spin coating for the fabrication of thin films. We exploited this behavior for the fabrication of BHJ-OSC devices incorporating **1a** and **1s** as acceptor material in the active layer. Except for the best PCE value of 1.73% obtained with centrosymmetrical *anti* isomer **1a**, *syn* isomer **1s** displays a slightly higher average PCE value, which might reflect the role of molecular symmetry on solid-state packing and thin film morphology. At this stage, however, device fabrication was unoptimized and the in-depth thin film characterization would deserve further investigation. This study underlines the potential of the di(benz[*f*]indenone)-fused tetraazaanthracene platform for the development of tailored electron acceptor molecules and *n*-type semiconducting organic materials.

EXPERIMENTAL SECTION

General Methods. All solvents for synthesis were of analytical grade. Electrochemical and spectroscopic measurements were carried out using spectroscopy grade solvents. FT-IR spectra of neat powders were recorded on an Agilent Cary 630 FT-IR instrument equipped with attenuated total reflectance (ATR) sampling. NMR spectra were recorded at room temperature on a JEOL JNM ECS 400 instrument (400 and 100 MHz for ^1H and ^{13}C , respectively). Structural assignments were made with additional information from gCOSY, gHMBC, and gHMBC experiments. Data are listed in parts per million and are reported relative to tetramethylsilane (^1H); residual solvent peaks of the deuterated solvents were used as an internal standard. The multiplicity of signals is designated by the following abbreviations: s, singlet; d, doublet; m, multiplet. Coupling constants *J* are reported in hertz. High-resolution mass spectrometry (HR-MS) was performed on a SYNAPT G2 HDMS instrument (Waters) using electrospray ionization (ESI) in positive mode and time-of-flight (TOF) mass analysis. Preparative HPLC separation was performed using an Agilent 1260 Infinity unit (pump G1311C, autosampler G1329B, DAD G1365D, and fraction collector G1364C), monitored by an Agilent OpenLAB CDS Chemstation LC instrument. The preparative column (250 mm \times 10 mm, 5 μm) used is a (S,S)-Whelk-O1. Elution was performed with a hexane/ethanol/dichloromethane mixture [70:20:10 (v/v)] as the mobile phase at a flow rate of 1 mL/min with UV detection (254 nm). Solution samples were filtered on a 0.45 μm PTFE filter prior to injection.

Synthesis of 9. A mixture of 4,9-diphenylbenz[*f*]indan-1,3-dione **8** (651 mg, 1.87 mmol) and *N*-bromosuccinimide (665 mg, 3.74 mmol) in ethanol (8 mL) and chloroform (8 mL) was stirred for 1 h at room temperature under Ar. The reaction was then quenched with 45 mL of water, and the mixture was extracted with dichloromethane (3 \times 40 mL). The collected organic layers were washed with brine (50 mL), dried over MgSO_4 , and concentrated *in vacuo* to give **9** as a yellow solid, which was directly used without further purification (1.01 g, crude yield of 99%): mp 93–98 $^\circ\text{C}$ dec; ^1H NMR (400 MHz, 298 K , CDCl_3) δ 7.92 (dd, 2H, *J* = 6.5, 3.3 Hz), 7.67 (dd, 2H, *J* = 6.5, 3.3 Hz), 7.64–7.56 (m, 6H), 7.46–7.38 (m, 4H).

Synthesis of 3. To a solution of **9** (939 mg, 1.86 mmol) in toluene (10.5 mL) was added 10 mL of DMSO at room temperature under Ar. The reaction mixture was stirred for 3.5 h at 90 $^\circ\text{C}$ using a heating mantle. After the mixture was cooled to room temperature, the reaction was quenched with water (80 mL) and the mixture extracted with EtOAc (3 \times 50 mL). The collected organic layers were dried over MgSO_4 and concentrated *in vacuo*. The crude product was purified via silica gel column chromatography eluting with a petroleum ether/EtOAc mixture [1:1 (v/v)] to afford **3** as a yellow solid (700 mg, 99% from crude **9**): mp 128 $^\circ\text{C}$; FT-IR 3421, 3057, 2923, 2866, 1720, 1443, 1372, 1204, 1179, 1147, 1041, 1009, 773, 736, 697 cm^{-1} ; ^1H NMR (400 MHz, 298 K , CDCl_3) δ 7.90 (dd, 2H, *J* = 6.5, 3.3 Hz), 7.65 (dd, 2H, *J* = 6.5, 3.3 Hz), 7.59–7.56 (m, 6H), 7.43–7.38 (m, 4H), 4.04 (broad s, 2H); $^{13}\text{C}\{^1\text{H}\}$ NMR (100 MHz,

298 K , CDCl_3) δ 194.4, 141.9, 136.9, 135.2, 130.0, 129.7, 129.2, 128.8, 128.7, 128.5, 86.6; HR-MS (ESI-TOF) *m/z* [$\text{M} + \text{Na}$] $^+$ calcd for $\text{C}_{25}\text{H}_{16}\text{O}_4\text{Na}^+$ 403.0941, found 403.0939.

Synthesis of 1a and 1s. A mixture of **3** (677 mg, 1.78 mmol) and **4** (429 mg, 0.86 mmol) in ethanol (9 mL) was refluxed using a heating mantle for 4.5 h under Ar. After the mixture had been cooled to room temperature, the reaction was quenched with water (12 mL) and the mixture extracted with dichloromethane (3 \times 40 mL) and EtOAc (20 mL). The collected organic layers were dried over MgSO_4 and concentrated *in vacuo*. The crude product was purified with silica gel column chromatography eluting with a petroleum ether/dichloromethane mixture [5:5 to 2:8 (v/v)] to give two main fractions. The first contained a mixture of **1a** and **1s** (1:1 molar ratio) as a brown solid (50 mg, 5%). The second fraction was a mixture of **2a** and **2s** (1:1 molar ratio) as an orange solid (455 mg, 44%).

A mixture of **2a** and **2s** (216 mg, 0.18 mmol) in acetic acid (20 mL) was then refluxed using a heating mantle for 3.5 h under Ar. The reaction mixture was neutralized with aqueous NaHCO_3 and then extracted with dichloromethane (2 \times 40 mL) and EtOAc (20 mL). The combined organic layers were dried over MgSO_4 and concentrated *in vacuo*. The crude product was purified with silica gel column chromatography eluting with a petroleum ether/dichloromethane mixture [1:1 (v/v)] to afford **1a** and **1s** (116 mg, 55%).

Small quantities of **1a** and **1s** isomers can be separated under those conditions, and the remaining mixture can be separated by preparative HPLC. This mixture (56 mg) was dissolved in a dichloromethane/hexane mixture [1:1 (v/v)], and the solution was subjected to HPLC affording pure isomers **1a** and **1s**. Aliquots (80 \times 200 μL) were injected every 6.6 min.

Mixture of 2a and 2s. Mp 285 $^\circ\text{C}$; FT-IR 3483, 3367, 3058, 2940, 2863, 1719, 1466, 1369, 1191, 1116, 1072, 989, 957, 881, 767, 737, 697, 669 cm^{-1} ; ^1H NMR (400 MHz, 298 K , CD_2Cl_2) δ 7.74 (d, 1H, *J* = 8.3 Hz), 7.69–7.36 (m, 25H), 7.29 (d, 1H, *J* = 7.1 Hz), 7.16 (d, 1H, *J* = 7.5 Hz), 5.98 (s, 1H, NH), 5.71 (s, 1H, NH), 4.27 (s, 1H, OH), 3.87 (s, 1H, OH), 1.25–0.92 (m, 42H); $^{13}\text{C}\{^1\text{H}\}$ NMR (100 MHz, 298 K , CD_2Cl_2) δ 194.4, 189.4, 156.4, 146.5, 143.2, 141.5, 141.3, 140.9, 138.9, 138.4, 137.9, 137.64, 137.55, 137.1, 136.84, 136.80, 136.5, 136.2, 135.6, 135.2, 133.8, 132.7, 130.99, 130.95, 130.8, 130.6, 130.4, 130.11, 130.05, 129.9, 129.8, 129.6, 129.50, 129.48, 129.46, 129.0, 128.9, 128.81, 128.76, 128.7, 128.6, 128.54, 128.45, 128.3, 128.0, 127.9, 127.3, 125.8, 106.5, 105.5, 104.8, 102.8, 100.5, 99.5, 84.3, 82.8, 19.5, 19.3, 19.13, 19.11, 11.9, 11.8; HR-MS (ESI-TOF) *m/z* [$\text{M} + \text{H}$] $^+$ calcd for $\text{C}_{78}\text{H}_{75}\text{N}_4\text{O}_4\text{Si}_2^+$ 1187.5321, found 1187.5310.

1a: HPLC [(S,S)-Whelk-O1, 70:20:10 *n*-heptane/ethanol/dichloromethane, flow rate of 1.0 mL/min, λ = 254 nm] t_{R} = 4.70 min; mp >300 $^\circ\text{C}$ dec; FT-IR 3059, 2941, 2863, 1729, 1610, 1581, 1444, 1376, 1184, 1150, 1115, 1087, 1013, 883, 777, 740, 699, 664 cm^{-1} ; ^1H NMR (400 MHz, 298 K , CDCl_3) δ 7.76 (d, 2H, *J* = 8.1 Hz), 7.69 (d, 2H, *J* = 8.1 Hz), 7.64–7.43 (m, 24H), 1.40–1.28 (septuplet, 6H, *J* = 7.2 Hz), 1.19 (d, 36H, *J* = 7.2 Hz); $^{13}\text{C}\{^1\text{H}\}$ NMR (100 MHz, 298 K , CDCl_3) δ 187.0, 156.8, 152.1, 145.1, 142.3, 141.3, 139.4, 137.6, 136.0, 135.6, 135.3, 131.4, 130.7, 130.2, 129.9, 129.6, 129.4, 128.7, 128.61, 128.58, 128.53, 128.51, 128.4, 125.3, 113.2, 101.0, 19.2, 12.0; HR-MS (ESI-TOF) *m/z* [$\text{M} + \text{H}$] $^+$ calcd for $\text{C}_{78}\text{H}_{71}\text{N}_4\text{O}_2\text{Si}_2^+$ 1151.5110, found 1151.5114.

1s: HPLC [(S,S)-Whelk-O1, 70:20:10 *n*-heptane/ethanol/dichloromethane, flow rate of 1.0 mL/min, λ = 254 nm] t_{R} = 7.28 min; mp >300 $^\circ\text{C}$ dec; FT-IR 3055, 2937, 2918, 2860, 1725, 1725, 1613, 1582, 1505, 1443, 1373, 1172, 1150, 1113, 1012, 958, 882, 772, 738, 697, 674 cm^{-1} ; ^1H NMR (400 MHz, 298 K , CD_2Cl_2) δ 7.78 (d, 2H, *J* = 8.3 Hz), 7.75 (d, 2H, *J* = 8.1 Hz), 7.68–7.46 (m, 24H), 1.25–1.14 (m, 24H), 1.03 (d, 18H, *J* = 7.2 Hz); $^{13}\text{C}\{^1\text{H}\}$ NMR (100 MHz, 298 K , CD_2Cl_2) δ 187.9, 157.7, 152.1, 145.3, 142.9, 141.9, 140.0, 137.9, 136.34, 136.29, 135.9, 132.0, 131.3, 131.2, 130.2, 129.8, 129.2, 129.0, 128.94, 128.92, 128.85, 128.84, 126.7, 123.7, 114.1, 112.6, 102.6, 100.8, 19.4, 19.1, 12.0, 11.8; HR-MS (ESI-TOF) *m/z* [$\text{M} + \text{H}$] $^+$ calcd for $\text{C}_{78}\text{H}_{71}\text{N}_4\text{O}_2\text{Si}_2^+$ 1151.5110, found 1151.5110.

Electrochemistry and Optical Spectroscopies. Cyclic voltammetry was performed using a BAS 100 Potentiostat (Bioanalytical Systems), and the data were analyzed with BAS100W version 2.3. A Pt working electrode (diameter of 1.6 mm), a Pt counter electrode, and a leak-free Ag/AgCl reference electrode with a 5 mm diameter were used. Cyclic voltammograms were recorded at a scan rate of 100 mV s⁻¹ for solutions of the compounds (concentration of ~5 × 10⁻⁴ M) in dichloromethane containing *n*-Bu₄NPF₆ (0.1 M) as the supporting electrolyte. Ferrocene was used as an internal standard [*E*^o(Fc/Fc⁺) = 0.46 V/SCE]. UV–vis absorption spectra were recorded on Varian Cary 50 and a dual-beam JASCO V670 spectrophotometer. Fluorescence and phosphorescence emission spectra were recorded on a FluoroLog-3 instrument (Jobin Yvon HORIBA iHR 320) equipped with a xenon lamp ensuring excitation wavelengths between 280 and 850 nm. Low-temperature spectra were recorded with the same apparatus using a quartz Dewar flask filled with liquid nitrogen.

Single-Crystal X-ray Diffraction. The intensity data for the single-crystal X-ray-diffraction analysis were collected on a Rigaku Oxford Diffraction SuperNova diffractometer at 120 K for **2s** and at room temperature for **1a** by using Cu K α radiation (λ = 1.54184 Å). Data collection reduction and multiscan ABSPACK correction were performed with CrysAlisPro (Rigaku Oxford Diffraction). Using Olex2,³⁰ the structures were determined by intrinsic phasing methods with SHELXT,³¹ and SHELXL³² was used for full-matrix least-squares refinement. A small mask of solvent was applied during the refinement of **1a** (void volume of 268.45 Å³). All H atoms were found experimentally and refined as riding atoms with their *U*_{iso} parameters constrained to 1.2*U*_{eq} (parent atom) for the aromatic atoms and to 1.5*U*_{eq} (parent atom) for the methyl groups and water molecules. CCDC 2121172 for **1a** and 2121173 for **2s** contain supplementary crystallographic data and can be obtained free of charge from the Cambridge Crystallographic Data Centre.

Thin Film Preparation. Glass substrates were consecutively cleaned by sonication in deionized water, in acetone, and in isopropanol, followed by a 15 min UV–ozone plasma treatment. Then, substrates were transferred into a N₂-filled glovebox. **1a** and **1s** solutions were prepared in chloroform at a concentration of 10 mg/mL and stirred overnight at 50 °C. The organic solutions were spin-coated with a spin-coater machine from SET Co. (model TP 6000) onto the substrates at 1500 rpm. Active layers with a thickness of 100–500 nm were obtained (measured by a stylus profilometer Bruker DEKTAK XT with a 1 mg force on the probing tip).

Device Fabrication. Donor/acceptor inks were prepared in a total concentration of 20 mg/mL (1:1 weight ratio) in chlorobenzene and stirred at 60 °C overnight. ITO-coated glass substrates (sheet resistance 10–15 Ω) purchased from LUMTEC were sequentially cleaned with deionized water, acetone, and isopropanol under sonication for 15 min each, dried with argon, and then treated in a UV–ozone oven for 15 min at 80 °C. All of the devices were fabricated in an ITO/ZnO/active layer/MoO₃/Ag inverted structure.²⁸ A ZnO layer was spin-coated in air from a 1% (v/v) solution in isopropanol at 5000 rpm followed by thermal annealing at 120 °C for 10 min. The substrates were then transferred to a N₂-filled glovebox where a blend film with a 50–100 nm thickness was spin-coated on top of ZnO films. Finally, 5 nm MoO₃ and 100 nm Ag were deposited by thermal evaporation through a mask to define an active area of 0.27 cm². The current density–voltage characterization of the devices under an AM1.5G light solar simulator (Newport Sol3A Class AAA) was performed with a Keithley 238 source meter unit inside the glovebox. The illumination intensity of the light source was calibrated to be 100 mW/cm² using a standard silicon solar cell (Newport Company, Oriel no. 94043A) calibrated by the National Renewable Energy Laboratory (NREL). Organic field effect transistors specially optimized for the investigation of charge transport in simple processed unipolar bottom gate bottom contact structures based on *n*-type materials were fabricated following a published procedure.³³

Computational Details. The theoretical calculations were performed with Gaussian16.A03 using default algorithms, procedures, and convergence thresholds.³⁴ Both **1a** and **1s** were modeled by

replacing the Si(iPr) capping groups with hydrogen atoms for obvious computational reasons. The ground-state geometries were optimized at the PCM(DCM)-M06³⁵/6-311G(d) level, and we checked that the minimal structures were true minima (absence of an imaginary frequency) at the very same level of theory. We then simulated the vertical absorption spectra using TD-DFT³⁶ and more precisely the PCM(DCM)-M06/6-311+G(2d,p) level, using the LR-PCM approach in its non-equilibrium limit to couple the solvent model to TD-DFT. This level of theory was also used to plot the electron density difference (EDD) using the total excited-state density obtained for the relevant states. Finally, in an effort to model vibronic effects, we again used the PCM(DCM)-M06/6-311+G(2d,p) approach to compute forces at the FC point, which allowed us to estimate vibrational couplings in the so-called vertical gradient (VG) approximation.³⁷ We used a broadening function with a HWHM of 300 cm⁻¹. The ground-state geometries of **2s** were calculated at the B3LYP/6-31g(d) level.

Accession Codes

CCDC 2121172–2121173 contain the supplementary crystallographic data for this paper. These data can be obtained free of charge via www.ccdc.cam.ac.uk/data_request/cif, or by emailing data_request@ccdc.cam.ac.uk, or by contacting The Cambridge Crystallographic Data Centre, 12 Union Road, Cambridge CB2 1EZ, UK; fax: +44 1223 336033.

■ AUTHOR INFORMATION

Corresponding Authors

Denis Jacquemin – Université de Nantes, CNRS, CEISAM UMR 6230, 44000 Nantes, France; orcid.org/0000-0002-4217-0708; Email: Denis.Jacquemin@univ-nantes.fr

Elena Zaborova – Aix Marseille Univ, CNRS, CINaM UMR 7325, AMUtech, 13288 Marseille, France; Email: elena.zaborova@univ-amu.fr

Frédéric Fages – Aix Marseille Univ, CNRS, CINaM UMR 7325, AMUtech, 13288 Marseille, France; orcid.org/0000-0003-2013-0710; Email: frederic.fages@univ-amu.fr

Authors

Bruno Salgues – Aix Marseille Univ, CNRS, CINaM UMR 7325, AMUtech, 13288 Marseille, France

Rudraditya Sarkar – Université de Nantes, CNRS, CEISAM UMR 6230, 44000 Nantes, France

Muhammad Luthfi Fajri – Aix Marseille Univ, CNRS, CINaM UMR 7325, AMUtech, 13288 Marseille, France

Yatzil Alejandra Avalos-Quiroz – Aix Marseille Univ, CNRS, CINaM UMR 7325, AMUtech, 13288 Marseille, France

Anne-Doriane Manick – Aix Marseille Univ, CNRS, Centrale Marseille, iSm2, UMR 7313, AMUtech, 13288 Marseille, France

Michel Giorgi – Aix Marseille Univ, CNRS, Centrale Marseille, FSCM, Spectropole, 13397 Marseille, France; orcid.org/0000-0002-4367-1985

Nicolas Vanthuyne – Aix Marseille Univ, CNRS, Centrale Marseille, iSm2, UMR 7313, AMUtech, 13288 Marseille, France; orcid.org/0000-0003-2598-7940

Yannick Carissan – Aix Marseille Univ, CNRS, Centrale Marseille, iSm2, UMR 7313, AMUtech, 13288 Marseille, France; orcid.org/0000-0002-9876-0272

Christine Vidélot-Ackermann – Aix Marseille Univ, CNRS, CINaM UMR 7325, AMUtech, 13288 Marseille, France; orcid.org/0000-0001-8240-6474

Jörg Ackermann – Aix Marseille Univ, CNRS, CINaM UMR 7325, AMUtech, 13288 Marseille, France

Gabriel Canard – Aix Marseille Univ, CNRS, CINaM UMR 7325, AMUtech, 13288 Marseille, France; orcid.org/0000-0002-3572-9091

Jean-Luc Parrain – Aix Marseille Univ, CNRS, Centrale Marseille, iSm2, UMR 7313, AMUtech, 13288 Marseille, France

Boris Le Guennic – Univ Rennes, CNRS, ISCR, UMR 6226, 35000 Rennes, France; orcid.org/0000-0003-3013-0546

Muriel Amatore – Aix Marseille Univ, CNRS, Centrale Marseille, iSm2, UMR 7313, AMUtech, 13288 Marseille, France; orcid.org/0000-0002-6455-5633

Laurent Commeiras – Aix Marseille Univ, CNRS, Centrale Marseille, iSm2, UMR 7313, AMUtech, 13288 Marseille, France; orcid.org/0000-0003-4331-6198

Notes

The authors declare no competing financial interest.

ACKNOWLEDGMENTS

The project leading to this publication has received funding from Excellence Initiative of Aix-Marseille University-A*MIDEX, a French “Investissement d’Avenir” program. This work was also supported by Aix Marseille Université and CNRS AMU, which the authors gratefully acknowledge. R.S. and D.J. thank the Region des Pays de la Loire for financial support in the framework of the OPT-BASIS project. R.S. and D.J. are indebted to the CCIPL-GliCid computational center installed in Nantes for the always generous allocation of computational time.

REFERENCES

(1) Fukuzumi, S.; Ohkubo, K. Organic Synthetic Transformations Using Organic Dyes as Photoredox Catalysts. *Org. Biomol. Chem.* **2014**, *12*, 6059–6071.
(2) Quinn, J. T. E.; Zhu, J.; Li, X.; Wang, J.; Li, Y. Recent progress in the development of n-type organic semiconductors for organic field effect transistors. *J. Mater. Chem. C* **2017**, *5*, 8654–8681.
(3) Hou, J.; Inganäs, O.; Friend, R. H.; Gao, F. Organic Solar Cells Based on Non-Fullerene Acceptors. *Nat. Mater.* **2018**, *17*, 119–128.
(4) Anthony, J. E.; Facchetti, A.; Heeney, M.; Marder, S. R.; Zhan, X. n-Type Organic Semiconductors in Organic Electronics. *Adv. Mater.* **2010**, *22*, 3876–3892.

(5) Nielsen, C. B.; Holliday, S.; Chen, H.-Y.; Cryer, S. J.; McCulloch, I. Non-fullerene Electron Acceptors for Use in Organic Solar Cells. *Acc. Chem. Res.* **2015**, *48*, 2803–2812.

(6) Bunz, U. H. F.; Freudenberg, J. N-Heteroacenes and N-Heteroarenes as N-Nanocarbon Segments. *Acc. Chem. Res.* **2019**, *52*, 1575–1587.

(7) Li, J.; Zhang, Q. Linearly Fused Azaacenes: Novel Approaches and New Applications Beyond Field-Effect Transistors (FETs). *ACS Appl. Mater. Interfaces* **2015**, *7*, 28049–28062.

(8) Anthony, J. E. Functionalized Acenes and Heteroacenes for Organic Electronics. *Chem. Rev.* **2006**, *106*, 5028–5048.

(9) Ahmed, E.; Earmme, T.; Ren, G.; Jenekhe, S. A. Novel n-Type Conjugated Ladder Heteroarenes: Synthesis, Self-Assembly of Nanowires, Electron Transport, and Electroluminescence of Bisindenoanthrazolines. *Chem. Mater.* **2010**, *22*, 5786–5796.

(10) Liu, H.; Mu, J.; Lee, J. Y. Charge Transport Properties of Stacking Bisindenoanthrazolines: DFT Studies. *J. Phys. Chem. B* **2011**, *115*, 8409–8416.

(11) Zhang, X.-Y.; Zhao, G.-J. Anisotropic Charge Transport in Bisindenoanthrazoline-Based n-Type Organic Semiconductors. *J. Phys. Chem. C* **2012**, *116*, 13858–13864.

(12) Ding, F.; Xia, D.; Ge, C.; Kang, Z.; Yang, Y.; Fan, R.; Lin, K.; Gao, X. Indenone-Fused N-Heteroacenes. *J. Mater. Chem. C* **2019**, *7*, 14314–14319.

(13) Chen, H.; Cai, G.; Guo, A.; Zhao, Z.; Kuang, J.; Zheng, L.; Zhao, L.; Chen, J.; Guo, Y.; Liu, Y. Low Band Gap Donor–Acceptor Conjugated Polymers with Indanone-Condensed Thiadiazolo[3,4-g]Quinoxaline Acceptors. *Macromolecules* **2019**, *52*, 6149–6159.

(14) Nishida, J.-I.; Deno, H.; Ichimura, S.; Nakagawa, T.; Yamashita, Y. Preparation, Physical Properties and n-Type FET Characteristics of Substituted Diindenopyrazinediones and Bis(dicyanomethylene) Derivatives. *J. Mater. Chem.* **2012**, *22*, 4483–4490.

(15) Wang, Z.-Y.; Dai, Y.-Z.; Ding, L.; Dong, B.-W.; Jiang, S.-D.; Wang, J.-Y.; Pei, J. A Stable Triplet-Ground-State Conjugated Diradical Based on a Diindenopyrazine Skeleton. *Angew. Chem., Int. Ed.* **2021**, *60*, 4594–4598.

(16) Zhu, L.; Ding, G.; Xie, L.; Cao, X.; Liu, J.; Lei, X.; Ma, J. Conjugated Carbonyl Compounds as High-Performance Cathode Materials for Rechargeable Batteries. *Chem. Mater.* **2019**, *31*, 8582–8612.

(17) Liu, D.-W.; Zhang, Y.; Li, X.-Y.; Xiao, Q.; Sun, W.-J.; Shao, X.; Zhang, H.-L. Nonvolatile Organic Field-Effect Transistor Memory from Pyrene-Fused Azaindacene Isomers. *J. Mater. Chem. C* **2021**, *9*, 6560–6567.

(18) Jones, D. W.; Pomfret, A.; Wife, R. L. o-Quinonoid Compounds. Part 18. Stabilised 2,3-Naphthoquinodimethanes via Transient 1,3-Diphenylbenz[f]inden-2-one. *J. Chem. Soc. Perkin Trans. 1* **1983**, *7*, 459–465.

(19) Heffner, R.; Safaryn, J. E.; Joullié, M. M. A New Synthesis of Benzo[f]Ninhydrin. *Tetrahedron Lett.* **1987**, *28*, 6539–6542.

(20) Luo, L.; Meng, L.; Sun, Q.; Ge, Z.; Li, R. Novel Synthesis of Thiazolo/Thienoazepine-5,8-Diones from Dihalo Cyclic 1,3-Diketones and Mercaptonitrile Salts. *RSC Adv.* **2014**, *4*, 6845–6849.

(21) Wang, E.; Hou, L.; Wang, Z.; Hellström, S.; Mammo, W.; Zhang, F.; Inganäs, O.; Andersson, M. R. Small Band Gap Polymers Synthesized via a Modified Nitration of 4,7-Dibromo-2,1,3-Benzothiadiazole. *Org. Lett.* **2010**, *12*, 4470–4473.

(22) De Cicco, R. C.; Black, A.; Li, L.; Goroff, N. S. An Iterative Method for the Synthesis of Symmetric Polyynes. *Eur. J. Org. Chem.* **2012**, *2012*, 4699–4704.

(23) An, C.; Zhou, S.; Baumgarten, M. Condensed Derivatives of Thiadiazoloquinoxaline as Strong Acceptors. *Cryst. Growth Des.* **2015**, *15*, 1934–1938.

(24) Wagner, C.; Hübner, O.; Kaifer, E.; Himmel, H.-J. Probing the Proton-Coupled Electron-Transfer (PCET) Reactivity of a Cross-Conjugated Cruciform Chromophore by Redox-State-Dependent Fluorescence. *Chem. - Eur. J.* **2019**, *25*, 3781–3785.

(25) Amer, A. M.; El-Bahnasawi, A. A.; Mahran, M. R. H.; Lapib, M. On the Synthesis of Pyrazino[2,3-b]Phenazine and 1H-Imidazo[4,5-b]Phenazine Derivatives. *Monatsh. Chem.* **1999**, *130*, 1217–1225.

(26) Djurovich, P. I.; Mayo, E. I.; Forrest, S. R.; Thompson, M. E. Measurement of the Lowest Unoccupied Molecular Orbital Energies of Molecular Organic Semiconductors. *Org. Electron.* **2009**, *10*, 515–520.

(27) Brosius, V.; Müller, M.; Borstelmann, J.; Rominger, F.; Freudenberg, J.; Bunz, U. H. F. Azaacenodibenzosuberones. *J. Org. Chem.* **2020**, *85*, 296–300.

(28) Perkhun, P.; Köntges, W.; Pourcin, F.; Esteouille, D.; Barulina, E.; Yoshimoto, N.; Pierron, P.; Margeat, O.; Videlot-Ackermann, C.; Bharwal, A. K.; Duché, D.; Herrero, C. R.; Gonzales, C.; Guerrero, A.; Bisquert, J.; Schröder, R. R.; Pfannmöller, M.; Ben Dkhil, S.; Simon, J.-J.; Ackermann, J. High-Efficiency Digital Inkjet-Printed Non-Fullerene Polymer Blends Using Non-Halogenated Solvents. *Adv. Energy Sustainability Res.* **2021**, *2*, 2000086.

(29) Zhang, S.; Ye, L.; Zhao, W.; Liu, D.; Yao, H.; Hou, J. Side Chain Selection for Designing Highly Efficient Photovoltaic Polymers with 2D-Conjugated Structure. *Macromolecules* **2014**, *47*, 4653–4659.

(30) Dolomanov, O. V.; Bourhis, L. J.; Gildea, R. J.; Howard, J. A. K.; Puschmann, H. OLEX2: a Complete Structure Solution, Refinement and Analysis Program. *J. Appl. Crystallogr.* **2009**, *42*, 339–341.

(31) Sheldrick, G. M. SHELXT - Integrated Space-Group and Crystal-Structure Determination. *Acta Crystallogr., Sect. A* **2015**, *71*, 3–8.

(32) Sheldrick, G. M. Crystal Structure Refinement with SHELXL. *Acta Crystallogr.* **2015**, *C71*, 3–8.

(33) Avalos-Quiroz, Y. A.; Koganezawa, T.; Perkhun, P.; Barulina, E.; Ruiz, C. M.; Ackermann, J.; Yoshimoto, N.; Videlot-Ackermann, C. Exploring Charge Transport in High Temperature Polymorphism of ITIC Derivatives in Simple Processed Unipolar Bottom Contact Organic Field Effect Transistor. *Adv. Elec. Mater.* **2021**, *8*, 2100743.

(34) Frisch, M. J.; Trucks, G. W.; Schlegel, H. B.; Scuseria, G. E.; Robb, M. A.; Cheeseman, J. R.; Scalmani, G.; Barone, V.; Petersson, G. A.; Nakatsuji, H.; Li, X.; Caricato, M.; Marenich, A. V.; Bloino, J.; Janesko, B. G.; Gomperts, R.; Mennucci, B.; Hratchian, H. P.; Ortiz, J. V.; Izmaylov, A. F.; Sonnenberg, J. L.; Williams-Young, D.; Ding, F.; Lipparini, F.; Egidi, F.; Goings, J.; Peng, B.; Petrone, A.; Henderson, T.; Ranasinghe, D.; Zakrzewski, V. G.; Gao, J.; Rega, N.; Zheng, G.; Liang, W.; Hada, M.; Ehara, M.; Toyota, K.; Fukuda, R.; Hasegawa, J.; Ishida, M.; Nakajima, T.; Honda, Y.; Kitao, O.; Nakai, H.; Vreven, T.; Throssell, K.; Montgomery, J. A., Jr.; Peralta, J. E.; Ogliaro, F.; Bearpark, M. J.; Heyd, J. J.; Brothers, E. N.; Kudin, K. N.; Staroverov, V. N.; Keith, T. A.; Kobayashi, R.; Normand, J.; Raghavachari, K.; Rendell, A. P.; Burant, J. C.; Iyengar, S. S.; Tomasi, J.; Cossi, M.; Millam, J. M.; Klene, M.; Adamo, C.; Cammi, R.; Ochterski, J. W.; Martin, R. L.; Morokuma, K.; Farkas, O.; Foresman, J. B.; Fox, D. J. *Gaussian 16*, rev. A.03; Gaussian, Inc.: Wallingford, CT, 2016.

(35) Zhao, Y.; Truhlar, D. G. The M06 Suite of Density Functionals for Main Group Thermochemistry, Thermochemical Kinetics, Noncovalent Interactions, Excited States, and Transition Elements: Two New Functionals and Systematic Testing of Four M06-Class Functionals and 12 Other Functionals. *Theor. Chem. Acc.* **2008**, *120*, 215–241.

(36) Adamo, C.; Jacquemin, D. The Calculations of Excited-State Properties with Time-Dependent Density Functional Theory. *Chem. Soc. Rev.* **2013**, *42*, 845–856.

(37) Santoro, F.; Jacquemin, D. Going Beyond the Vertical Approximation with Time-Dependent Density Functional Theory. *WIREs Comput. Mol. Sci.* **2016**, *6*, 460–486.